

# On the nature of the anomalous event in 2021 in the dwarf nova SS Cygni and its multi-wavelength transition

Mariko KIMURA,<sup>1,\*</sup> Shinya YAMADA,<sup>2</sup> Nozomi NAKANIWA,<sup>3</sup> Yoshihiro MAKITA,<sup>2</sup> Hitoshi NEGORO,<sup>4</sup> Megumi SHIDATSU,<sup>5</sup> Taichi KATO,<sup>6</sup> Teruaki ENOTO,<sup>1</sup> Keisuke ISOGAI,<sup>7,8</sup> Tatehiro MIHARA,<sup>1</sup> Hidehiko AKAZAWA,<sup>9</sup> Keith C. GENDREAU,<sup>10</sup> Franz-Josef HAMBSCH,<sup>11,12,13</sup> Pavol A. DUBOVSKY,<sup>14</sup> Igor KUDZEJ,<sup>14</sup> Kiyoshi KASAI,<sup>15</sup> Tamás TORDAI,<sup>16</sup> Elena PAVLENKO,<sup>17,18</sup> Aleksei A. SOSNOVSKIY,<sup>17</sup> Julia V. BABINA,<sup>17</sup> Oksana I. ANTONYUK,<sup>17</sup> Hiroshi ITOH,<sup>19</sup> and Hiroyuki MAEHARA <sup>7,20,21</sup>

<sup>1</sup>Cluster for Pioneering Research, Institute of Physical and Chemical Research (RIKEN), 2-1 Hirosawa, Wako, Saitama 351-0198, Japan

<sup>2</sup>Department of Physics, Rikkyo University, 3-34-1 Nishi-Ikebukuro, Toshima-ku, Tokyo 171-8501, Japan

<sup>3</sup>Department of Physics, Tokyo Metropolitan University, 1-1 Minami-Osawa, Hachioji, Tokyo 192-0397, Japan

<sup>4</sup>Department of Physics, Nihon University, 1-8 Kanda-Surugadai, Chiyoda-ku, Tokyo 101-8308, Japan

<sup>5</sup>Department of Physics, Ehime University, 2-5, Bunkyocho, Matsuyama, Ehime 790-8577, Japan

<sup>6</sup>Department of Astronomy, Graduate School of Science, Kyoto University, Oiwakecho, Kitashirakawa, Sakyo-ku, Kyoto, Kyoto 606-8502, Japan

<sup>7</sup>Okayama Observatory, Kyoto University, 3037-5 Honjo, Kamogatacho, Asakuchi, Okayama 719-0232, Japan

<sup>8</sup>Department of Multi-Disciplinary Sciences, Graduate School of Arts and Sciences, The University of Tokyo, 3-8-1 Komaba, Meguro, Tokyo 153-8902, Japan

<sup>9</sup>Akazawa Funao Observatory, 107 Funao, Funaocho, Kurashiki, Okayama 710-0261, Japan

<sup>10</sup>Astrophysics Science Division, NASA Goddard Space Flight Center, Greenbelt, MD 20771, USA

<sup>11</sup>Groupe Européen d'Observations Stellaires (GEOS), 23 Parc de Levesville, 28300 Bailleau l'Evêque, France

<sup>12</sup>Bundesdeutsche Arbeitsgemeinschaft für Veränderliche Sterne (BAV), Munsterdamm 90, 12169 Berlin, Germany

<sup>13</sup>Vereniging Voor Sterrenkunde (VVS), Oude Bleken 12, 2400 Mol, Belgium

<sup>14</sup>Vihorlat Observatory, Mierova 4, 06601 Humenne, Slovakia

<sup>15</sup>Baselstrasse 133D, CH-4132 Muttens, Switzerland

<sup>16</sup>Polaris Observatory, Hungarian Astronomical Association, Laborc utca 2/c, 1037 Budapest, Hungary

<sup>17</sup>Federal State Budget Scientific Institution “Crimean Astrophysical Observatory of RAS”, Nauchny, 298409, Republic of Crimea

<sup>18</sup>V. I. Vernadsky Crimean Federal University, 4 Vernadskogo Prospekt, Simferopol, 295007, Republic of Crimea

<sup>19</sup>Variable Star Observers League in Japan (VSOLJ), 1001-105 Nishiterakata-machi, Hachioji, Tokyo 192-0153, Japan

<sup>20</sup>Subaru Telescope Okayama Branch Office, National Astronomical Observatory of Japan, National Institutes of Natural Sciences, 3037-5 Honjo, Kamogata, Asakuchi, Okayama 719-0232, Japan

<sup>21</sup>Variable Star Observers League in Japan (VSOLJ), Okayama, Japan

\*E-mail: [mkimura@kustastro.kyoto-u.ac.jp](mailto:mkimura@kustastro.kyoto-u.ac.jp)

Received 2021 April 28; Accepted 2021 June 28

## Abstract

SS Cyg has long been recognized as the prototype of a group of dwarf novae that show only outbursts. However, this object has entered a quite anomalous event in 2021, which at first appeared to be standstill, i.e., an almost constant luminosity state observed in Z Cam-type dwarf novae. This unexpected event gives us a great opportunity to reconsider the nature of standstill in cataclysmic variables. We have observed this anomalous event and its forerunner, a gradual and simultaneous increase in the optical and X-ray flux during quiescence, through many optical telescopes and the X-ray telescopes NICER and NuSTAR. We have not found any amplification of the orbital hump during quiescence before the anomalous event, which suggests that the mass transfer rate did not significantly fluctuate on average. The estimated X-ray flux was not enough to explain the increment of the optical flux during quiescence via X-ray irradiation of the disk and the secondary star. It would be natural to consider that viscosity in the quiescent disk was enhanced before the anomalous event, which increased mass accretion rates in the disk and raised not only the optical flux but also the X-ray flux. We suggest that enhanced viscosity also triggered the standstill-like phenomenon in SS Cyg, which is considered to be a series of small outbursts. The inner part of the disk would always stay in the outburst state and only its outer part would be unstable against the thermal–viscous instability during this phenomenon, which is consistent with the observed optical color variations. This scenario is in line with our X-ray spectral analyses which imply that the X-ray-emitting inner accretion flow became hotter than usual and vertically expanded, and that it became denser and was cooled down after the onset of the standstill-like state.

**Key words:** accretion, accretion disks — novae, cataclysmic variables — stars: dwarf novae — stars: individual (SS Cygni)

## 1 Introduction

Cataclysmic variables (CVs) are close binary systems composed of a primary white dwarf (WD) and a secondary low-mass cool star. The secondary star provides its mass to the disk by Roche-lobe overflow and an accretion disk is formed around the WD. Dwarf novae (DNe), one subclass of CVs, show intermittent outbursts which are the sudden brightening of the disk. For a general review, see Warner (1995).

It is widely accepted that thermal–viscous instability triggered by partial ionization of hydrogen causes dwarf-nova outbursts, and this model is called “the disk-instability model” (for reviews, see Cannizzo 1993b; Osaki 1996; Hameury 2020). In this model, the thermal equilibrium curve of a given radius of the disk has an unstable state sandwiched by two stable states: the hot state corresponding to the outburst state with a high accretion rate, and the cool state corresponding to the quiescent state with a low

accretion rate (Meyer & Meyer-Hofmeister 1981). If a local region of the disk jumps between these two stable states, transition waves propagate and alter the thermal state of the entire disk at once (e.g., Smak 1984; Mineshige & Osaki 1985).

The basic assumption in the disk-instability model is that the mass transfer rate from the secondary star is constant. The mass transfer rate is one of the system parameters for the classification of DNe. If it is less than the critical rate, denoted as  $\dot{M}_{\text{crit}}$ , above which the disk is thermally stable, the systems repeat outbursts and are called SS Cyg-type stars. If the mass transfer rate exceeds  $\dot{M}_{\text{crit}}$ , the systems show no eruptive events and are called nova-like stars (NLs). If the mass transfer rate is close to and fluctuates around  $\dot{M}_{\text{crit}}$ , the systems alternate between frequent dwarf-nova outbursts and standstill, i.e., a state having constant luminosity in between that of outburst and quiescence. They are named Z Cam-type stars and regarded as the intermediate class between SS Cyg-type stars and NLs.

The alternation between standstill and outbursts in Z Cam-type stars cannot be understood by the simple disk-instability model and it is believed that fluctuations of transfer rates are necessary (e.g., Meyer & Meyer-Hofmeister 1983; Buat-Ménard et al. 2001). Ross and Latter (2017) attempted to reproduce the Z Cam-type phenomenon by fluctuations of the turbulent viscosity without variations in mass transfer rates, but they failed to generate long-lasting standstills and several consecutive outbursts. We thus have not yet explained all of the dwarf-nova outbursts by the simple disk-instability model, so that the disk-instability model should be sublimated towards a truly unified model that can explain a wide variety of light variations in DNe.

SS Cyg is the brightest DN over various wavelengths. This system has been monitored by visual observations and optical telescopes for more than 100 years (see the AAVSO historical light curve<sup>1</sup>) and has constantly repeated normal dwarf-nova outbursts with amplitudes of  $\sim 3.5$  mag and with intervals of  $\sim 1$  month in the long history of optical observations. This source has thus been the prototype of SS Cyg-type stars. However, it has entered a state of anomaly that we have never seen before since the end of 2021 January. This event seemed to be a genuine standstill at first sight (vsnet-alert 25453)<sup>2</sup> and was completely unexpected. SS Cyg may no longer be the prototype of SS Cyg-type stars.

This anomalous event in SS Cyg was accompanied by its predecessor phenomenon, which is the gradual and simultaneous increase in the optical and X-ray flux in the quiescent state. This phenomenon started around 2019 August. X-ray monitoring has continued for more than 20 years,<sup>3</sup> but the long-lasting increase of the system brightness was the first X-ray event. We noticed this multi-wavelength transition towards the anomalous event in 2021 and have monitored this source at optical and X-ray wavelengths since 2020 via the Variable Star Network (VSNET) collaboration team, the American Association of Variable Star Observers (AAVSO) (Waagen 2020), the Neutron star Interior Composition Explorer (NICER; Gendreau et al. 2016), and the Nuclear Spectroscopic Telescope Array (NuSTAR; Harrison et al. 2013).

It is not obvious why SS Cyg, in which the mass transfer rate is not close to the critical rate, should exhibit a standstill-like phenomenon. The present event in SS Cyg may therefore give some important suggestions to a long-standing question in the study of dwarf-nova outbursts: Are mass-transfer-rate fluctuations necessary to reproduce

standstill? We also may have to reconsider the nature of standstill in CVs. Our primary goal is to understand what causes the unexpected event and its transition in SS Cyg by analyzing multi-wavelength data. Simultaneously, the increase in the X-ray flux gives us a good opportunity to explore the inner accretion flow which is not well investigated (for a review, see Balman 2020). Section 2 describes our optical and X-ray observations. Section 3 shows the results of our data analyses. We discuss the cause of the anomalous event in 2021 and its multi-wavelength transition, and provide the entire accretion picture, in section 4. A summary is given in section 5.

## 2 Observations and data reduction

### 2.1 Optical photometry

Time-resolved CCD photometric observations of SS Cyg were carried out by the VSNET collaboration team and AAVSO. The log of the observation by the VSNET team is given in table E1.<sup>4</sup> We use the AAVSO archive data<sup>5</sup> in the  $B$ ,  $V$ ,  $R_C$ , and  $I_C$  bands after BJD 2453396. We convert all of the observation times to barycentric Julian date (BJD) in terrestrial time (TT). The data reduction and the calibration of the comparison stars were performed by each observer. The constancy of each comparison star was checked by nearby stars in the same images. The magnitude of each comparison star was measured by the AAVSO Photometric All-Sky Survey (APASS; Henden et al. 2016) from the AAVSO Variable Star Database.<sup>6</sup>

### 2.2 NICER

NICER has monitored SS Cyg since 2020 May. We use part of the data taken in optical quiescence during the 2021 anomalous event and its pre-stage, whose periods are defined in subsection 3.1. The corresponding ObsIDs are given in table E2. In this work, we utilize HEASoft version 6.27.2 for data reduction and analyses. The data were reprocessed with the pipeline tool `nicer12` based on the NICER Calibration Database (CALDB) version later than 2019 May 16, before producing light curves and time-averaged spectra of the individual ObsIDs. The background spectra are extracted by `nibackgen3C50` version 6. For spectral analyses, we obtained the response matrix file and the

<sup>1</sup> <https://www.aavso.org/sites/default/files/images/historicLC-SSCyg.jpg>.

<sup>2</sup> <http://ooruri.kuastro.kyoto-u.ac.jp/pipermail/vsnet-alert/>.

<sup>3</sup> <http://maxi.riken.jp/pubdata/v3/J2142+435/index.html>;  
<http://xte.mit.edu/asmlc/srcs/sscyg.html>.

<sup>4</sup> Tables E1–E4 and figures E1–E6 are available in the supplementary data section of the online edition of this article.

<sup>5</sup> <http://www.aavso.org/data/download/>.

<sup>6</sup> <http://www.aavso.org/vsp>.

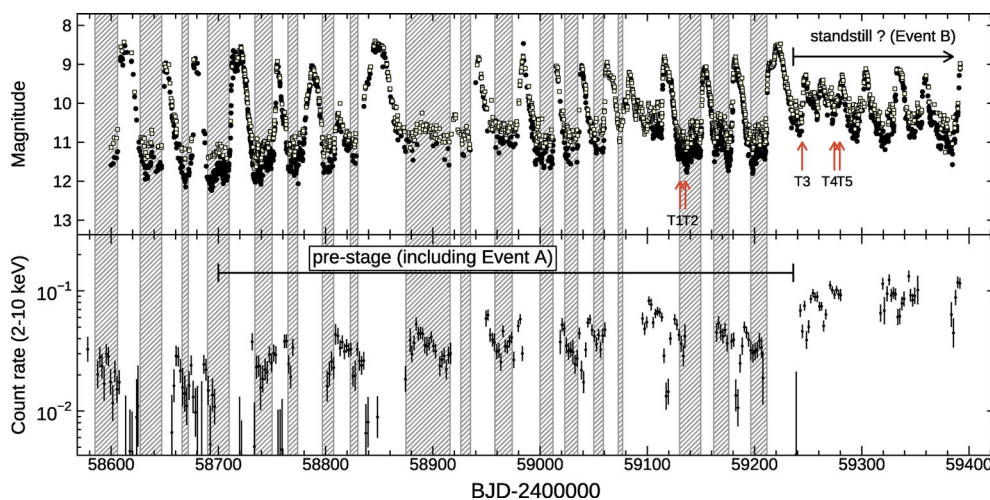


**Fig. 1.** Long-term optical and X-ray light curves. The upper panel exhibits optical light curves taken by the AAVSO and the VSNET observers. The photometric data are binned to 0.1 d. The circles and squares represent the V-band and  $R_C$ -band photometry, respectively. The lower panel shows the MAXI light curve for 2–10 keV. The data are binned to 2 d. We denote the time periods of the optical quiescence by the shaded regions. In the upper panel, the arrows indicate the dates when coordinated observations with NICER and NuSTAR were performed. (Color online)

ancillary response file for a specific set of 50 detectors to match the default settings of the background model.<sup>7</sup>

### 2.3 NuSTAR

NuSTAR target of opportunity (ToO) observations were coordinated by some of the NICER observations. The ObsIDs of these observations that we use in this paper are given in table E3. The data are reprocessed through *nupipeline* and the NuSTAR CALDB as of 2021 April 27. The light curves, time-averaged spectra, and response and ancillary response files are obtained by *nuproducts*. If the source is bright, we sometimes need the multi-layer insulation (MLI) correction (Madsen et al. 2020) for the FPMA data.<sup>8</sup> We extracted the FPMA spectra of the ObsIDs 90701304002, 90702309002, and 90702309004 by using the old ancillary response file. The background region is extracted as a circular region with a radius of  $80''$  at a blank sky area. We determine the source region as a circular region centered on the target with a  $100''$ – $120''$  radius by considering the time-varying brightness of the target.

## 3 Results of optical and X-ray analyses

### 3.1 Overall optical and X-ray light curves

First of all, we show the long-term optical and X-ray light curves in figure 1. The X-ray light curves that we use here are Monitor of All-sky X-ray Image (MAXI; Matsuoka et al. 2009) Gas Slit Camera (GSC) light curves, which are

retrieved through the on-demand system.<sup>9</sup> In this figure, we indicate the time periods of the optical quiescent state by the shaded regions. We see that the optical and X-ray flux began increasing around BJD 2458700 in the optical quiescent state. The  $R_C$ -band light curve during just the quiescent state is given in figure E1. The mean flux in the quiescent state seems to have continuously increased at two wavelengths until the onset of the long outburst triggered on BJD 2459210, though it modulated on timescales of  $\sim 100$  d. After the long outburst, the system showed small amplitude fluctuations. We define the time period between BJD 2458700 and BJD 2459236 as the pre-stage and the gradual increase in the optical and X-ray fluxes in the hatched time intervals of the optical quiescent state during the pre-stage as Event A. We also define the anomalous event which is possibly similar to standstill after BJD 2459236 as Event B.

The optical luminosity increased by  $\sim 1$  mag during Event A. The optical outbursts observed in SS Cyg are roughly classified into two types: short outbursts with small amplitudes and long outbursts with large amplitudes. These outbursts show steep rises and they are considered to be triggered at the outer disk, i.e., outside-in outbursts, and the long outburst and the short outburst are repeated alternately (Cannizzo & Mattei 1998). The slow-rise outbursts are likely inside-out outbursts, which are triggered at the inner region of the disk, and relatively rare events (see the AAVSO historical light curve). However, the slow-rise and small-amplitude outbursts occurred frequently, especially after BJD 2458700. Also, anomalous outbursts with very low amplitudes sometimes occurred in the pre-stage.

<sup>7</sup> The method is described at ([https://heasarc.gsfc.nasa.gov/docs/nicer/analysis\\_threads/arf-rmf/](https://heasarc.gsfc.nasa.gov/docs/nicer/analysis_threads/arf-rmf/)), and we use the additional data version xti20200722.

<sup>8</sup> ([https://nustarsoc.caltech.edu/NuSTAR\\_Public/NuSTAROperationSite/mli.php](https://nustarsoc.caltech.edu/NuSTAR_Public/NuSTAROperationSite/mli.php)).

<sup>9</sup> (<http://maxi.riken.jp/mxondem/>).



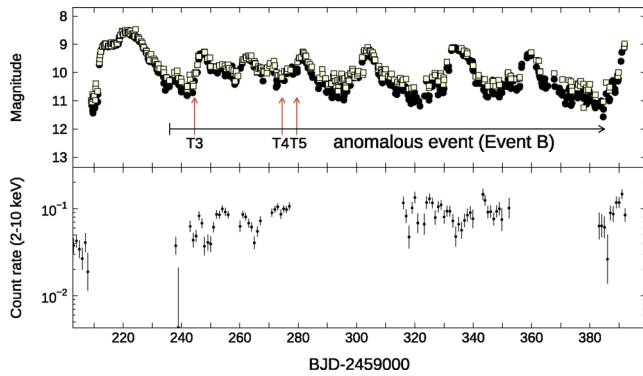


**Fig. 2.** Recent activity of SS Cyg. These panels are the same as the upper and lower panels of figure 1, but after the onset of the 2021 long outburst. In the lower panel, the data are binned to 1 d. (Color online)

The X-ray flux temporarily drops in the optical outburst state, which is consistent with the observations reported by Wheatley, Mauche, and Mattei (2003) and McGowan, Priedhorsky, and Trudolyubov (2004).

We next focus on the light curves around Event B in figure 2. SS Cyg entered a precursor outburst on BJD 2459210. Its precursor has a shoulder-like shape and lasted for  $\sim 5$  d before the outburst maximum. Although the precursor is sometimes observed at the beginning of long outbursts in SS Cyg-type stars (Cannizzo 2012; Ramsay et al. 2012), the duration is mostly a couple of days. The precursor in this outburst is therefore extremely long. Also, we do not see a clear plateau stage in this long outburst, though the long outburst in SS Cyg normally has a gradually decaying plateau stage during  $\sim 1$  week before the fading to the quiescent level. This long outburst faded around BJD 2459230 and SS Cyg entered a standstill-like phenomenon with oscillatory variations since BJD 2459236. Although a similar event might have occurred in 1908 in this source, the period when the quiescent level was rising is around 100 d, which is shorter than that of the pre-stage, and the anomalous event in 1908 looks like a group of  $\sim 2$  mag-amplitude small outbursts (see figure E2). Also, similar multi-wavelength behavior was seen around BJD 2459100. However, the event after BJD 2459236 is more anomalous and long-lasting. The optical luminosity is considered to approximately represent the gravitational energy released from the disk via mass accretion. We average the V-band light curves per day and derive the mean luminosity before Event B to be  $\sim 10.3$  mag. The mean luminosity in Event B is  $\sim 10.1$  mag, which is comparable with that before Event B.<sup>10</sup>

<sup>10</sup> Here, the mean luminosity is averaged over fluxes and converted into magnitudes.

### 3.2 Optical orbital light curves

We show here the averaged  $R_C$ -band orbital light curve in the optical quiescence before the pre-stage and that in Event A in figure 3. For the data before the pre-stage, we extract the light curve fainter than 11 mag during BJD 2453868–2458700. We fold the  $R_C$ -band light curve with the orbital period of 0.27512973 d derived by Hsman (1986) and determine the orbital phase using the epoch BJD 2456190.62771 reported by Hill et al. (2017), which corresponds to the inferior conjunction of the secondary star. Before folding light curves, we subtract the long-term trend of light curves from the observational data by locally weighted polynomial regression (LOWESS; Cleveland 1979).

The orbital light curve in the optical quiescence before the pre-stage, which is exhibited in the left panel of figure 3, can be interpreted as the superposition of the orbital hump and the ellipsoidal modulation. The orbital hump originates from the bright spot created at the disk outer rim by the collision between the gas stream from the secondary star and the disk, and appears around the orbital phase of  $\sim 0.8$ . This is because the bright spot rotates with the binary orbital motion and is hidden from the observer when the secondary star is behind the optically thick disk (see, e.g., Wood et al. 1986). The ellipsoidal modulation is generated by the change in the projection area of the distorted secondary star to the observer and peaks at the orbital phases of 0.25 and 0.75 (see, e.g., Allan et al. 1996). Since the inclination angle of SS Cyg is measured to be  $45^\circ$  (Hill et al. 2017), these two effects are observable and the disk and the WD are not eclipsed.

Comparing the left and the right panels of figure 3, we see that the flux amplitude of the hump with a peak around phase 0.8, which is measured from the light minimum around phase 0.0, does not significantly change. Although both the ellipsoidal modulation and the orbital hump contribute to this hump, we find no observational evidence that the luminosity of the secondary star changes much during Event A (see also subsection 4.1). Therefore, the flux amplitude in the orbital hump would not change on average during Event A, which means that the bright spot in Event A is as bright as that in the quiescent state before the pre-stage. On the other hand, the hump around orbital phase 0.3 in the right panel may originate from X-ray irradiation of the secondary star. As estimated in subsection 4.1, the temperature of the irradiated surface of the secondary star increases by a few percent at most in Event A. If we take into account that part of the irradiated surface is not seen to the observer around phase 0.0, a  $\sim 0.1$  mag hump is possible at most. This is enough to explain the amplitude of this hump. However, it is not straightforward to understand that the peak phase of this hump deviates from 0.5.

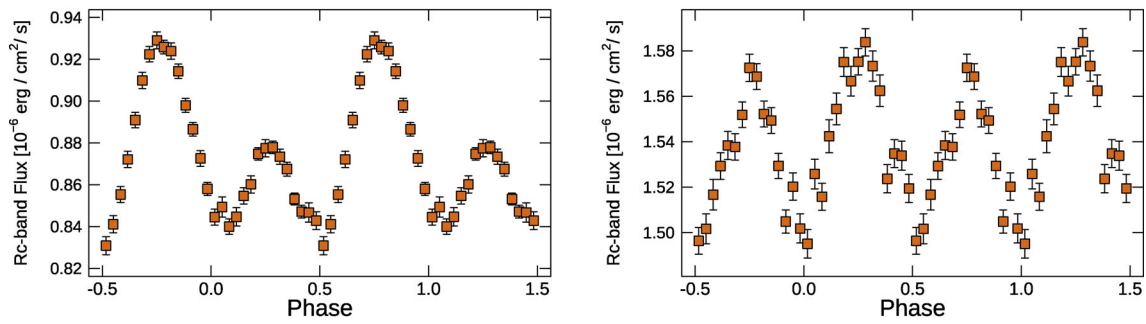


Fig. 3. Orbital light curves in the  $R_C$  band. The left and the right panels are the orbital profile in the optical quiescence before the pre-stage and that in Event A, respectively. (Color online)

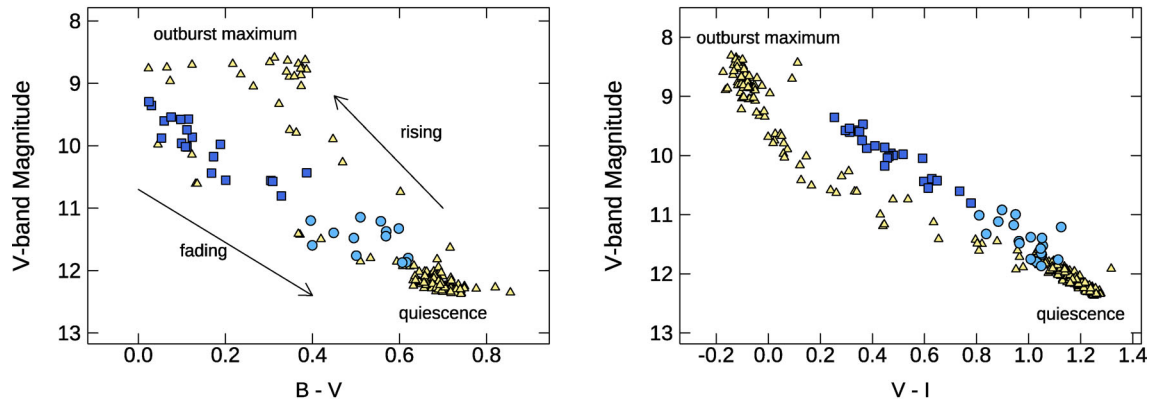


Fig. 4. Optical color variations with respect to the  $V$ -band magnitude. The left and right panels show the  $B - V$  and  $V - I$  color variations, respectively. The triangles, circles, and squares represent the data during normal long outbursts between BJD 2456130 and BJD 2456280, those in Event A, and those in Event B, respectively. (Color online)

Although this phenomenon was also detected in another CV (Kimura et al. 2020a), its interpretation is unclear. One possibility is that the part of the outer edge of the disk that collides with the gas stream from the secondary star, i.e., the location of the bright spot, is geometrically thicker than the rest of the outer edge of the disk, making the irradiated surface of the secondary star asymmetric with respect to the line connecting the WD and the secondary star. In this case, part of the X-ray radiation would be interrupted by the thicker part and the observable area of the irradiated surface of the secondary star would be maximized at an orbital phase earlier than 0.5.

### 3.3 Optical color variations

We explore here the optical color variations. We average the light curves per orbital cycle and extract the colors. We select the data of the two normal long outbursts between BJD 2456130 and BJD 2456280 for this analysis as in figure 2 of Hameury et al. (2020) and compare the color variations in Events A and B. The  $1\sigma$  errors are typically around 0.1 mag, and we exclude data with errors greater than 0.2 mag. Also, we use the simultaneous observation data and exclude data with a mean orbital phase

of 0.75–0.85 to avoid the significant influence of the high-temperature bright spot on the color.

The  $B - V$  color variation with respect to the  $V$ -band magnitude is displayed in the left panel of figure 4. As described in Hameury et al. (2020), the color of SS Cyg normally evolves counterclockwise with time through one outburst cycle in this color–magnitude diagram (see the arrows in the left panel), and the  $B - V$  color in the normal quiescent state is around 0.7 (see the triangles). However, the  $B - V$  color became bluer in Event A and much bluer most of the time in Event B (see the circles and the squares). The color during Events A and B seems to be similar to that in the fading stage from the outburst maximum. At the fading stage, the cooling wave terminating an outburst is triggered at the outer disk and propagates inwards (Mineshige & Osaki 1985). The above-mentioned similarity implies that the inner region of the disk became hotter during Event A than in the normal quiescent state, and that the hot inner region was heated up further and/or occupied a larger area in the disk during Event B. Additionally, strong Balmer emission lines and the He II (4686) emission line were detected in the optical spectra taken in Event B (see figure E3). In comparison with the time

evolution of optical spectra in SS Cyg, which was reported by Hessman et al. (1984), these features are similar to those of optical spectra in the fading stage of the same system. We note here that all of the WD, the disk, the secondary star, and the bright spot contribute to the optical emission; however, the effect on the color variation by the change in the WD temperature is very small since the WD is tiny. Also, there is no observational evidence of a significant increase in the temperature of the secondary star. Moreover, we avoid the contamination of the bright spot.

We also show the  $V - I$  color variation with respect to the  $V$ -band magnitude in the right panel of figure 4. The  $V - I$  color evolves linearly in this diagram during normal long outbursts (see the triangles in the same panel). We see that this color became redder in Events A and B by  $\sim 0.2$  in comparison with the data in normal long outbursts. This may imply that the disk expanded in the radial direction in Events A and B. The typical disk spectrum is a multi-temperature blackbody and its Rayleigh–Jeans tail exists around optical and near-infrared wavelengths. That tail depends on the temperature of the outermost disk and the disk radius. The  $V - I$  color is more sensitive to them than the  $B - V$  color. The redder  $V - I$  color in Events A and B may therefore imply that the disk expanded in the radial direction and/or that the low-temperature component in the outer disk increased. The  $V - I$  colors of 0.5 and 1.0 correspond to blackbody radiation of  $\sim 7000$  K and  $\sim 5000$  K.

### 3.4 Broad-band X-ray spectra

#### 3.4.1 Model of multi-temperature plasma

Non-magnetic CVs including DNe harbor an X-ray-emitting region in the vicinity of the WD, in which the rotational energy of the matter transferred from the inner edge of the accretion disk is deposited to enable the gas to settle onto the slowly rotating WD. In the conventional picture, the X-ray-emitting region, named the boundary layer (BL), is optically thin with low accretion rates onto the WD, and becomes optically thick with high accretion rates and emits UV and soft X-ray photons (Narayan & Popham 1993; Patterson & Raymond 1985a, 1985b). However, recent X-ray spectral and timing analyses suggest that optically thin multi-temperature plasma emitting hard X-rays exists regardless of mass accretion rates. Although its structure and the mechanism for generating that region are controversial, an optically thin hot accretion flow like advection-dominated accretion flow (ADAF; Narayan & Yi 1994) sometimes merged with the BL may surround the WD and the accretion disk would be truncated apart from the WD surface (for a review, see Balman 2020). Here, we treat broad-band X-ray spectra during Events A and B, when the

accretion rate would not be very high, and simply call the X-ray-emitting region the BL.

We obtained five sets of broad-band X-ray spectra in the 0.5–50 keV range thanks to coordinated observations by NICER and NuSTAR (see also the arrows in the upper panel of figure 1) and attempt to fit these spectral energy densities (SEDs).<sup>11</sup> The broad-band spectra referred to as T1 and T2 in figure 5 were taken in Event A, and those referred to as T3, T4, and T5 were taken in Event B.

In evaluating the X-ray spectrum of non-magnetic CVs, the cooling flow model is practically adopted (e.g., Done & Osborne 1997; Ishida et al. 2009; Tsujimoto et al. 2018; Nakaniwa et al. 2019). In this paper we use the CEVMKL model in the XSPEC software (Arnaud 1996) for comparison with the spectral analyses of SS Cyg by Ishida et al. (2009). In this model, the expected spectrum is a sum of bremsstrahlung emissivity as follows:

$$L(\nu) \propto \int_{T_{bb}}^{T_{max}} \frac{\epsilon(T, n^2, \nu)}{\epsilon(T, n^2)} dT. \quad (1)$$

Here,  $\epsilon(T, n^2, \nu)$  is the bremsstrahlung spectral emissivity,  $\epsilon(T, n^2)$  is the total bremsstrahlung emissivity integrated over  $\nu$ , and  $T_{max}$  and  $T_{bb}$  are the shock temperature at the boundary between the disk and the BL and the blackbody temperature of the WD surface and/or the surface of the inner disk, respectively. The differential emission measure (DEM) in this model is proportional to a power-law function of temperature (Done et al. 1995) and given as

$$d(\text{EM}) \propto (T/T_{max})^\alpha d(\log T) \propto (T/T_{max})^{\alpha-1} dT \quad \text{for } T < T_{max}. \quad (2)$$

It is necessary to combine the CEVMKL model and the reflection model because the surface of the WD and/or the accretion disk subtends the BL, intercepts X-rays, and reflects some of them off into space (Done & Osborne 1997). Also, the GAUSSIAN model should be introduced to describe the fluorescence  $K\alpha$  line emission. We therefore fit the SEDs with the model TBABS \* (REFLECT \* CEVMKL + GAUSSIAN). We utilize XSPEC version 12.11.0. Here, the TBABS model is multiplied in order to account for the interstellar and possible intrinsic absorption of SS Cyg.

#### 3.4.2 Results of spectral modeling

As discussed by Ishida et al. (2009), the abundances of iron and oxygen in the CEVMKL model, which are denoted as  $Z_{Fe}$  and  $Z_O$ , affect very much the determination of the solid

<sup>11</sup> The NuSTAR spectrum extends to 80 keV, but we utilize the data for 3–50 keV because the intrinsic spectrum from SS Cyg is comparable with the background at  $>50$  keV. Also, the model that we use is limited to the energy band softer than  $\sim 50$  keV. We confirm that there is no hard energy tail in these spectra.

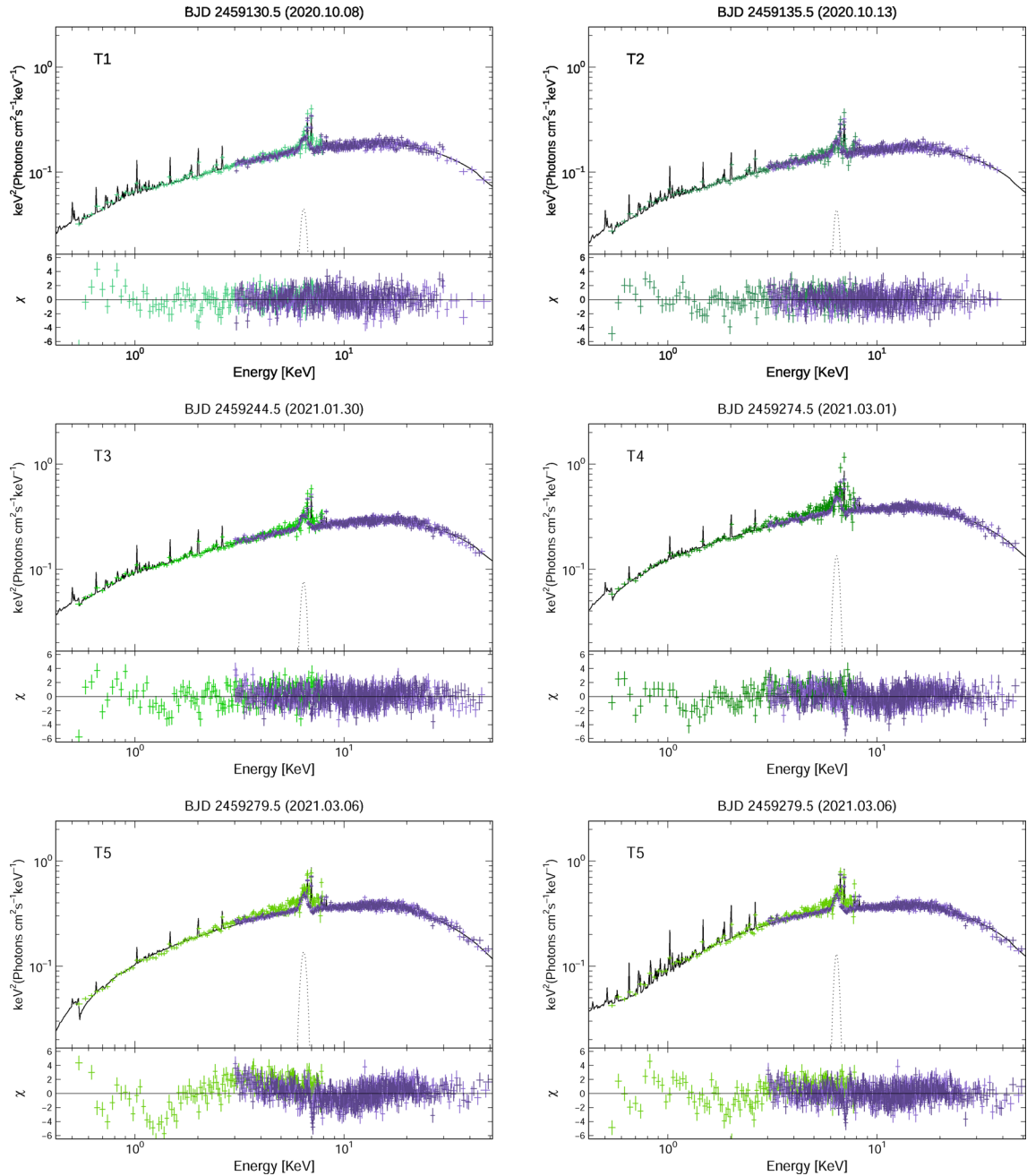


**Fig. 5.** Broad-band X-ray SEDs. The green crosses represent the observed NICER SEDs. The purple and dark purple crosses represent the observed NuSTAR FPMA and FPMB SEDs, respectively. The solid and dotted lines represent the emission reproduced by our model and the model emission from the fluorescence  $K\alpha$  line, respectively. (Color online)

angle of the reflector subtending the BL, which is denoted as  $\Omega/(2\pi)$ , and the plasma emission parameters  $T_{\max}$  and  $\alpha$  in equation (2). These abundances should be the same over the five datasets. Before analyzing each individual spectrum, we simultaneously fit all five datasets, tying  $Z_{\text{Fe}}$  and  $Z_{\text{O}}$  in the CEVMKL model. The abundances of Ca, Ar, S, Si, Mg, and Ne are fixed at the estimates by Ishida et al. (2009). The abundances of the other elements are fixed at solar values given in Anders and Grevesse (1989). The abundance and the iron abundance in the REFLECT model are tied to  $Z_{\text{O}}$  and

$Z_{\text{Fe}}$ , respectively. The line energy in the GAUSSIAN model is fixed at 6.4 keV. The hydrogen column density ( $N_{\text{H}}$ ) in the TBABS model,  $\Omega/(2\pi)$  in the REFLECT model,  $T_{\max}$ ,  $\alpha$ , and the normalization in the CEVMKL model, and the line width ( $\sigma$ ) and the normalization in the GAUSSIAN model, are free to vary. The inclination angle of the reflector is set to be that of the binary system,  $45^\circ$  (Hill et al. 2017). Here we use 114.25 pc as the distance to SS Cyg, obtained by the Gaia parallax (Bailer-Jones et al. 2018). Also, we add an offset in normalizations between the NICER and



**Table 1.** Best-fitting parameters of our modeling in the five sets of broad-band spectra. The errors represent 90% confidence ranges.

Model	Parameter	T1	T2	T3	T4	T5	T5
TBABS	$N_{\text{H}}^*$	$2.7 \pm 0.2$	$3.6 \pm 0.2$	$2.8 \pm 0.2$	$4.9 \pm 0.3$	$8.6 \pm 0.1$	—
PCFABS	$N_{\text{H}}^*$	—	—	—	—	—	$70.0 \pm 3.3$
	$f^\dagger$	—	—	—	—	—	$0.59 \pm 0.01$
REFLECTION	$\Omega/(2\pi)^\ddagger$	$0.27 \pm 0.04$	$0.28^{+0.05}_{-0.04}$	$0.23 \pm 0.03$	$0.15 \pm 0.03$	$0.10 \pm 0.02$	$0.25 \pm 0.03$
CEVMKL	$\alpha^\S$	$0.82 \pm 0.03$	$0.85 \pm 0.03$	$0.96 \pm 0.03$	$1.25^{+0.07}_{-0.06}$	$1.86 \pm 0.10$	$0.65 \pm 0.04$
	$T_{\text{max}}^\parallel$	$33.8 \pm 0.7$	$32.6^{+1.2}_{-1.1}$	$33.7 \pm 0.7$	$27.1 \pm 0.5$	$23.6 \pm 0.4$	$30.7 \pm 0.6$
	$N_1^\P$	$0.52 \pm 0.01$	$0.49 \pm 0.01$	$0.88 \pm 0.02$	$1.56 \pm 0.06$	$2.06 \pm 0.08$	$1.04^{+0.04}_{-0.03}$
GAUSSIAN	$\sigma^{**}$	$0.22 \pm 0.04$	$0.20 \pm 0.03$	$0.20 \pm 0.02$	$0.20 \pm 0.01$	$0.21 \pm 0.01$	$0.18 \pm 0.02$
	$N_2^{\dagger\dagger}$	$6.06^{+0.63}_{-0.59}$	$5.50^{+0.54}_{-0.52}$	$9.31^{+0.54}_{-0.53}$	$16.8^{+0.77}_{-0.76}$	$17.9 \pm 0.49$	$14.2^{+0.75}_{-0.74}$
$\chi^2/\text{dof}$		1.30	1.22	1.36	1.40	2.12	1.44
$L_{\text{X}}^{\dagger\dagger}$		$1.4 \times 10^{33}$	$1.2 \times 10^{33}$	$2.1 \times 10^{33}$	$2.8 \times 10^{33}$	$2.7 \times 10^{33}$	$2.7 \times 10^{33}$
Hardness $^{\S\S}$		1.21	1.21	1.23	1.19	1.21	1.18

\*Equivalent hydrogen column in units of  $10^{20}$  atoms  $\text{cm}^{-2}$ .

$^\dagger$ Dimensionless covering fraction ( $0 < f \leq 1$ ).

$^\ddagger$ Solid angle of cold matter surrounding the plasma.

$^\S$ Index for power-law emissivity function.

$^\parallel$ Maximum temperature in units of keV.

$^\P$ Normalization of the plasma model.

$^{**}$ Line width in units of keV.

$^{\dagger\dagger}$ Total photons  $\text{cm}^{-12} \text{s}^{-1}$  in the line of sight in units of  $10^{-4}$ .

$^{\ddagger\dagger}$ X-ray luminosity in the 1–50 keV band in units of  $\text{erg s}^{-1}$ .

$^{\S\S}$ Hardness ratio defined as the ratio of the flux in 6–15 keV to that in 2–6 keV.

NuSTAR SEDs in our fittings by considering uncertainties on the cross calibration and time variations of the emission from this source. The observational times by NICER and NuSTAR were not exactly the same in each coordinated observation and the X-ray flux of this source varies on timescales of hundreds of seconds. We also add a cross-normalization parameter between the NuSTAR FPMA and FPMB SEDs in T3–T5. As a result, the best-fitting values for  $Z_{\text{Fe}}$  and  $Z_{\text{O}}$  are 0.10 and 0.23, respectively. The normalization of the NICER SEDs is 0.83–1.02 times that of the NuSTAR SEDs. The normalization of the NuSTAR FPMB is 1.01–1.05 times that of the NuSTAR FPMA in T3–T5.

We next fit each individual SED by the same model with  $Z_{\text{Fe}}$  and  $Z_{\text{O}}$  fixed at the obtained values. The extracted best-fitting parameter values and their errors for each SED are summarized in table 1, and the SEDs and the models are displayed in figure 5. We also give the X-ray luminosity and the hardness ratio in the same table. Our modeling of these SEDs works well for the data of T1–T4. We see some excess for the SED in T5 in the softer energy band at less than 8 keV, and the fit is improved if we include the PCFABS model for partial absorption instead of the TBABS model (see the bottom panels of figure 5). The results are added in table 1.

According to the best-fitting parameters given in table 1, the solid angle subtended by the reflector is small for all SEDs. The maximum temperature of the BL exceeds 30 keV in T1–T3 and decreases in T4 and T5. The hardness ratio defined as the ratio of the flux in 2–6 keV to that in 6–15 keV is almost the same from T1 to T5. In comparison with the estimates by Wheatley, Mauche, and Mattei (2003) and Ishida et al. (2009), the X-ray luminosity increases by about double in T1 and T2, by around four times in T3, and by about five times in T4 and T5. The width of the fluorescence  $K\alpha$  line is obtained as  $\sim 0.2$  keV in all of the observations, though this is further investigated in sub-subsection 3.4.3 by using only the narrow energy range of the NICER data to avoid systematic uncertainties on the cross calibration and the simultaneous fitting of wide-band spectra.

The derived hydrogen column density of photoelectric absorption is much larger than the interstellar absorption of SS Cyg,  $3.0 \times 10^{19} \text{ cm}^{-2}$ , which was constrained by ultraviolet and optical spectroscopy (Mauche et al. 1988; Ritchey et al. 2013). This implies that additional material responsible for intrinsic absorption surrounds the BL. This absorption may change on timescales of around one week according to the results of SED fittings in T1 and T2 and those in T4 and T5, and seems to become larger from T3 to T5. The improvement of the SED fitting in T5 with the

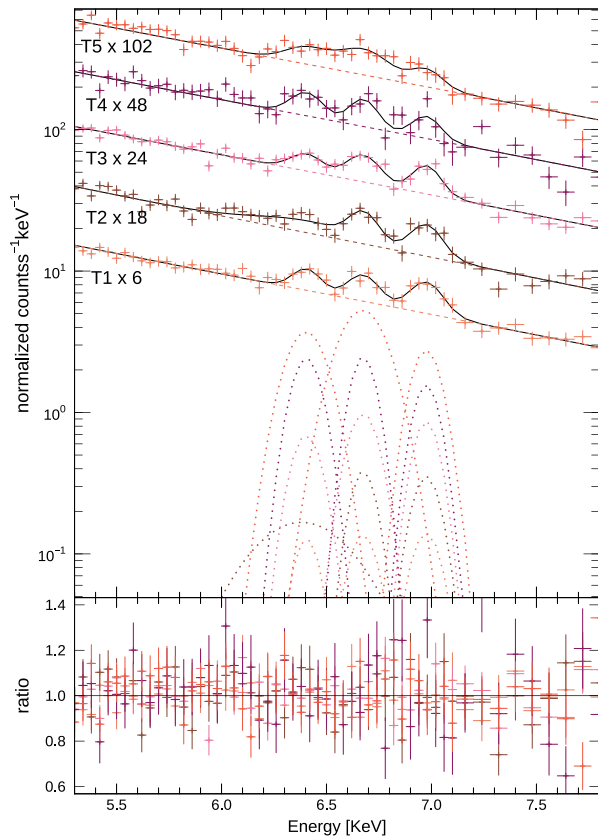


**Fig. 6.** Results of the model fitting by a power law plus three Gaussians. The solid, dashed, and dotted lines represent the emission reproduced by our model, the model continuum, and the model emissions from the three iron lines, respectively. Each observed spectrum and each continuum model are shifted in the vertical axis for visibility and their offsets are denoted at the left side of each spectrum. We set another offset for the three Gaussian models of each spectrum for visibility. (Color online)

model for partial absorption may suggest that the BL in T5 is partially masked by dense absorbers. Although the ionization degree of the absorber might change between T1 and T5, a detailed study is deferred to a forthcoming paper.

### 3.4.3 Iron emission lines

We next attempt to fit the NICER spectra for 5–8 keV by a model consisting of a power-law continuum and three Gaussian lines in order to evaluate the fluorescence, He-like, and H-like  $K\alpha$  iron emission lines. The central energy of the three Gaussian lines is fixed at 6.4, 6.67, and 6.97 keV. We set the lower limit of the line width at 1 eV because the energy resolution of the Silicon Drift Detector (SDD) on board NICER is 137 eV at 6 keV.<sup>12</sup> The fitting results are shown in figure 6. The best-fitting parameter values are given in table 2.

The width of the fluorescence line becomes broader in T5, although it is not well determined in T2. Part of the BL

is considered to cover the innermost region of the disk. If the 6.4 keV emission line originates from the reflection at the innermost disk, and if its line width is determined by the Keplerian velocity amplitude of the disk, the broader line width in T5 may imply that the inner disk edge gradually contracts just before T5. For example, the line width of  $0.078^{+0.067}_{-0.056}$  keV in T5 corresponds to an inner disk edge of  $(0.3\text{--}10) \times 10^9$  cm, which is roughly consistent with the estimate in subsection 3.5. The width of the He-like line seems to be broader in T5 than in the other time periods despite large error bars. The  $K\alpha$  photons reflected by the WD and/or the disk may suffer from Compton scattering as discussed in Hellier, Mukai, and Osborne (1998). Some  $K\alpha$  emission lines other than the three lines that we consider here might be mixed. Also, the H-like emission line seems to become weaker from T3 to T4. This may be consistent with the maximum temperature of the BL becoming lower in T4 and T5 in comparison with T1–T3 (see also table 1) since the flux ratio between H-like and He-like emission lines is sensitive to the temperature of the X-ray-emitting plasma in CVs and is expected to increase with increasing plasma temperature (Xu et al. 2019).

### 3.5 X-ray stochastic variability

The multi-wavelength light curves of some CVs are more or less dominated by stochastic variability referred to as “flickering” (for reviews, see Bruch 1992, 2021). The flickering in CVs, X-ray binaries, and active galactic nuclei is considered to be produced by fluctuations of mass accretion rates at different disk radii, which vary on local viscous timescales at each radius of the disk (Lyubarskii 1997; Yonehara et al. 1997; Uttley & McHardy 2001; Arévalo & Uttley 2006). The fluctuations propagate inwards and characterize the X-ray variability from the BL. It is known that the power spectrum (PS) of flickering has a broken power-law shape and the break frequency is considered to be associated with the dynamical timescale at the inner disk edge (e.g., Revnivtsev et al. 2010; Balman & Revnivtsev 2012), though other complex factors are related to it, as pointed out by Scaringi (2014). We therefore try to estimate the innermost radius of the accretion disk by using the break frequency of the PS of the X-ray light curves.

We have extracted light curves in the 0.3–7 keV band with 1 s bins during Events A and B from the NICER data and divided the light curve into several windows in which the data have equally spaced sampling times. We have used the publicly available Python library *Stingray* (Huppenkothen et al. 2019) for each window and obtained the PS. Here we normalize the power to squared fractional root mean square (Belloni & Hasinger 1990) and bin the

<sup>12</sup> ([https://heasarc.gsfc.nasa.gov/docs/nicer/nicer\\_tech\\_desc.html](https://heasarc.gsfc.nasa.gov/docs/nicer/nicer_tech_desc.html)).

**Table 2.** Best-fitting parameters of our modeling in the five sets of the NICER spectrum for 5–8 keV.\*

Model	Parameter	T1	T2	T3	T4	T5
Power law (continuum)	$\alpha^\dagger$	$1.6 \pm 0.2$	$1.7 \pm 0.2$	$1.6 \pm 0.1$	$1.5 \pm 0.1$	$1.5 \pm 0.2$
	$N_c^\ddagger$	$7.6^{+2.7}_{-1.9}$	$7.7^{+1.5}_{-1.2}$	$12.1^{+3.4}_{-2.6}$	$14.0 \pm 3.2$	$15.0^{+5.8}_{-4.0}$
Gaussian 1 (fluorescence)	$\sigma_1^\S$	$0.016^{+0.057}_{-0.016}$	$0.236^{+0.092}_{-0.064}$	$0.040^{+0.048}_{-0.040}$	$0.038^{+0.047}_{-0.038}$	$0.078^{+0.067}_{-0.056}$
	$N_1^\parallel$	$2.7^{+1.0}_{-0.8}$	$4.4 \pm 1.4$	$4.1^{+1.5}_{-1.3}$	$7.1 \pm 2.4$	$7.0^{+3.5}_{-4.9}$
	$EW_1^\#$	$60^{+24}_{-17}$	$115^{+85}_{-50}$	$53^{+21}_{-19}$	$74^{+45}_{-22}$	$65^{+31}_{-30}$
Gaussian 2 (He-like)	$\sigma_2^\S$	$0.032^{+0.044}_{-0.032}$	$0.001^{+0.042}_{-0.001}$	$0.040^{+0.030}_{-0.040}$	$0.001^{+0.064}_{-0.001}$	$0.094^{+0.117}_{-0.050}$
	$N_2^\parallel$	$3.5 \pm 1.0$	$2.9 \pm 0.7$	$6.6 \pm 1.5$	$7.0 \pm 1.7$	$12.7^{+9.4}_{-3.9}$
	$EW_2^\#$	$76^{+32}_{-22}$	$74 \pm 25$	$85^{+22}_{-19}$	$69^{+34}_{-25}$	$127^{+52}_{-40}$
Gaussian 3 (H-like)	$\sigma_3^\S$	$0.036^{+0.035}_{-0.036}$	$0.027^{+0.036}_{-0.027}$	$0.001^{+0.051}_{-0.001}$	$0.001^{+0.070}_{-0.001}$	$0.034^{+0.095}_{-0.033}$
	$N_3^\parallel$	$4.2 \pm 1.0$	$3.4 \pm 0.8$	$5.8 \pm 1.2$	$5.2 \pm 2.4$	$4.8 \pm 3.8$
	$EW_3^\#$	$109^{+33}_{-24}$	$98^{+35}_{-33}$	$84^{+19}_{-16}$	$49^{+33}_{-22}$	$52^{+43}_{-34}$
$\chi^2/\text{dof}$		0.48	1.06	0.93	1.12	1.05

\*The errors represent 90% confidence ranges.

$^\dagger$ Photon index of power-law  $\alpha$ .

$^\ddagger$ Total photons  $\text{cm}^{-2} \text{s}^{-1}$  in the line of sight of the continuum emission in units of  $10^{-2}$ .

$^\S$ Line width in units of keV.

$^\parallel$ Total photons  $\text{cm}^{-2} \text{s}^{-1}$  in the line of sight in units of  $10^{-4}$ .

$^\#$ Equivalent width in units of eV.

power with a logarithmic rebinning factor of 0.25 or 0.4. We fit each PS by the following equation:

$$P(\nu) = a\nu^{-1} \left[ 1 + \left( \frac{\nu}{b} \right)^4 \right]^{-1/4} + c, \quad (3)$$

where  $\nu$  is the frequency and  $P(\nu)$  is the power. The parameters  $a$ ,  $b$ , and  $c$  are free to vary in our fitting, and  $a$  and  $b$  represent the normalization and the break frequency, respectively. We introduce the parameter  $c$  to describe the white noise component. This equation is based on a simple analytical model of a truncated accretion disk (Revnivtsev et al. 2010), and here  $b$  is  $\sqrt{GM_1/r_{\text{in}}^3/(2\pi)}$ , where  $G$  is the gravitational constant,  $M_1$  is the WD mass, and  $r_{\text{in}}$  is the innermost radius of the accretion disk.

The results of our PS fitting and the estimation of the innermost radius of the disk are tabulated in Table E4. An example PS and the associated fitting results are displayed in figure 7, and the others are given in figures E4 and E5. Although some light variations other than flickering may be excited on short timescales, we simply assume here that the PS has a power-law shape. The innermost disk radius is estimated to be  $(3.5 \pm 0.3) \times 10^9 \text{ cm}$  by averaging the results for each PS during Event A. Although this value is slightly smaller than the averaged value during the normal quiescence before the pre-stage, which is  $\sim 5 \times 10^9 \text{ cm}$  (Balman & Revnivtsev 2012), our estimates are consistent with the idea that the disk is truncated far from the WD surface in the optical quiescence, which was proposed by Meyer and Meyer-Hofmeister (1994).

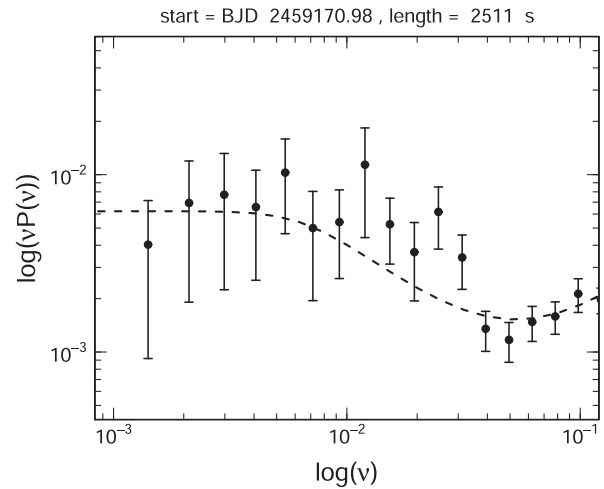


**Fig. 7.** Power spectrum and fitting result of the NICER light curve during BJD 2459170.9752–2459171.0043. The black points and bars penetrating them represent the powers multiplied by the frequencies and their 1  $\sigma$  errors. The dashed line represents the result of our fitting by using equation (3). The start time of the observation and the length of the window are given at the top of this panel.

It may be unclear whether or not the break frequency in PSs corresponds to the innermost disk radius; however, we obtain an anti-correlation between the size of the inner edge of the disk and the optical brightness during Event A as displayed in figure 8 despite large error bars (see the circles). This may imply that the inner disk edge extends toward the WD as the accretion rate of the disk increases. The WD radius is  $\sim 5 \times 10^8 \text{ cm}$  for a WD mass of  $0.94 M_\odot$ .

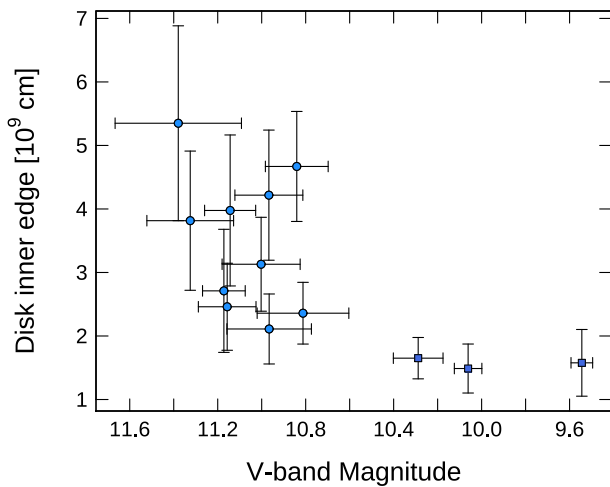


**Fig. 8.** Correlation between the estimated size of the inner edge of the accretion disk and the optical V-band magnitude. The circles and squares represent the estimates during Events A and B respectively. (Color online)

(Nauenberg 1972; Provencal et al. 1998; Hill et al. 2017). By contrast, the innermost disk radius appears to stay at a smaller value during Event B (see the squares in the same figure).

## 4 Discussion

### 4.1 Cause of the simultaneous increase in the optical and X-ray flux

Our ultimate goal is to understand why the anomalous event in 2021 in SS Cyg, Event B, was triggered. To achieve this purpose, it is essential to examine the cause of its multi-wavelength predecessor phenomenon which is the gradual increase in the optical flux in the quiescent state during the pre-stage, Event A. The following three scenarios should be discussed as the cause. The first possibility is an enhancement of mass transfer rates from the secondary star, which would also increase the X-ray flux after viscous timescales at the outer disk. The second possibility is that X-ray irradiation of the disk and the secondary star becomes stronger together with the increase in the X-ray flux. The third possibility is that the intrinsic flux of the disk increases.

First of all, we do not find any amplification of the orbital hump during Event A (see figure 3). The amplitude of the orbital hump in the flux scale should be enhanced if the luminosity of the bright spot, which is connected to the mass transfer rate, increases. There is no positive evidence that the mass transfer rate changes on average during Event A, at least in our observations, although we cannot rule out that the transfer rate might fluctuate within the error bars,  $\sim 5\%$ , on average and might temporarily vary. Also, the irradiation of the secondary star that we discuss later cannot greatly enhance the transfer rate (Osaki & Meyer 2004).

We next examine the X-ray irradiation of the disk and the secondary star. X-rays harder than  $\sim 1$  keV can heat the surface of the disk and the secondary star (Aller 1959; Cruddace et al. 1974). The X-ray luminosity in the 1–50 keV band is estimated to be  $\sim 1 \times 10^{33} \text{ erg s}^{-1}$  during Event A from our results in subsection 3.4 (see table 1). The X-ray albedo of the disk is  $\sim 0.9$  according to de Jong, van Paradijs, and Augusteijn (1996) and the scale height  $H$  is very small, i.e.,  $H/r$  is typically  $\sim 0.01$ . The X-ray flux which the disk surface receives is roughly estimated to be less than  $1 \times 10^{31} \text{ erg s}^{-1}$ . This is smaller than the expected intrinsic disk flux in the quiescent state by an order of magnitude (see, e.g., Smak 1984; Wheatley et al. 2003). Therefore, the irradiated disk emission would be trivial.

If the secondary star is irradiated by hard X-rays from the BL, its temperature is altered as

$$T_{2,\text{irr}}^4 = T_2^4 + (1 - \eta_s) L_X \frac{1}{4\pi a^2 \sigma}, \quad (4)$$

where  $T_{2,\text{irr}}$  and  $T_2$  are respectively the temperature of the irradiated secondary star and the intrinsic temperature of the secondary, which is estimated to be 4750 K (Hill et al. 2017) [see equation (1) of Hameury et al. 2020]. Also,  $\eta_s$  is the albedo of the secondary star, which is  $\sim 0.4$  (de Jong et al. 1996),  $L_X$  is the X-ray luminosity,  $a$  is the binary separation, and  $\sigma$  is the Stefan–Boltzmann constant (Hameury et al. 2020). By substituting the X-ray luminosity estimated from our SED fittings, we see that X-ray irradiation increases the temperature of the secondary star by only a few percent at most. Consequently, the irradiation of the disk and the secondary star would not be the main source of the increase in the optical flux.

As a result of the above considerations, the third possibility seems to be the most plausible. The accretion rate in the disk would increase, which leads to the brightening of the disk. According to Hameury et al. (2020), the optical emission from the disk plus the bright spot is about half of that from the secondary star during the normal quiescence in SS Cyg. To explain the optical luminosity during Event A, the disk should be brighter by  $\sim 1.6$  times than the secondary star. In particular, the inner part of the disk may be brighter on the basis of the  $B - V$  color during Event A, which is investigated in subsection 3.3 (see also the circles in the left panel of figure 4). The X-ray luminosity is roughly estimated by using the mass accretion rate at the inner disk edge ( $\dot{M}_{\text{in}}$ ):<sup>13</sup>

$$L_X \sim \frac{GM_1 \dot{M}_{\text{in}}}{2r_{\text{in}}}. \quad (5)$$

<sup>13</sup> We note that this equation may be replaced by other forms if the situation is more complex, e.g., the inner disk edge is truncated far from the WD surface and/or the truncated disk is covered by the X-ray-emitting coronal flow.



If the mass accretion is enhanced at the disk inner edge, the X-ray flux rises. We can thus understand not only the slow growth of the optical flux but also that of the X-ray flux in a consistent manner by enhanced mass accretion in the inner disk.

## 4.2 Enhanced viscosity in the quiescent disk

In the previous subsection we suggested that the increase in the mass accretion rate in the inner part of the disk may be responsible for the gradual increase in the optical and X-ray flux during Event A. We next consider the reason why the accretion rate increases. The local accretion rate at a given radius of the disk is expressed as  $\dot{M}(r) = 2\pi r \Sigma(-v_r)$ . Here,  $v_r$  is the radial velocity by the viscous diffusion and  $(-v_r) \sim \alpha_{\text{cool}} c_s^2 / v_K$  in the quiescent disk, where  $\alpha_{\text{cool}}$  is the viscous parameter in the cool state,<sup>14</sup>  $c_s$  is the sound velocity,  $v_K$  is the Keplerian velocity, and  $\Sigma$  is the surface density. The local accretion rate in the quiescent disk is therefore proportional to  $\alpha_{\text{cool}} r^{3/2} \Sigma_{\text{cool}} T_c$ , where  $T_c$  is the temperature at the equatorial plane of the disk. Here,  $\Sigma_{\text{cool}}$  is the surface density in the quiescent disk and it is larger than  $\Sigma_{\text{min}}$  typically by a factor of two. Since  $\Sigma_{\text{min}}$  is approximately proportional to  $r$  and  $\alpha_{\text{hot}}^{-0.8}$  (see, e.g., Hameury et al. 1998), the mass accretion rate at the inner disk edge in the quiescent state is roughly expressed as

$$\dot{M}_{\text{in}} \propto \alpha_{\text{cool}} \alpha_{\text{hot}}^{-0.8} T_c r_{\text{in}}^{2.5}. \quad (6)$$

The inner edge of the accretion disk during Event A would be comparable with or a little smaller than that in the normal quiescence according to our estimates in subsection 3.5. Therefore, the viscosity and the temperature would increase in the cool state in order to account for the increase in the optical and X-ray flux. If the viscosity in the cool state is enhanced, the viscous heating becomes more efficient, which makes the temperature of the disk higher. Cannizzo (1993a) showed that the quiescent level rises with the increase in  $\alpha_{\text{cool}}$  by performing numerical simulations.

The enhancement of viscosity in the cool state affects light curves as follows. It is considered that  $\alpha_{\text{cool}}$  should be lower than the viscosity in the hot state ( $\alpha_{\text{hot}}$ ) to reproduce a clear-cut cycle between the quiescent state and the outburst state as a result of numerical simulations by Smak (1984) and Mineshige and Osaki (1985). Also, outbursts tend to be triggered at the outer disk in the case where  $\alpha_{\text{cool}}$  increases as the radial distance from the WD becomes larger (Mineshige & Wood 1989), though outside-in outbursts are easily triggered if the mass transfer rate is high even without the radial dependence of  $\alpha_{\text{cool}}$

(Cannizzo et al. 1988; Ichikawa & Osaki 1994). If the viscosity in the cool state increases particularly at the inner disk, inside-out outbursts frequently occur and their amplitudes become smaller. Although it may be difficult to distinguish outside-in and inside-out outbursts only by optical light curves (Schreiber et al. 2003), some numerical simulations and recent eclipse analyses showed that the optical rise of inside-out outbursts tends to be slower in comparison with that of outside-in outbursts (Smak 1984; Cannizzo et al. 1986; Court et al. 2020). Also, long outbursts may be suppressed if more disk mass is drained to the WD during frequent short outbursts due to efficient angular momentum transfer in the disk. In fact, SS Cyg repeated small and slow-rise outbursts during Event A and showed no long outbursts during  $\sim 1.5$  yr before 2021 (see the upper panel of figure 1). This behavior may be evidence of the temporal enhancement of  $\alpha_{\text{cool}}$ .

It is difficult to understand the reason why the viscosity in the cool state is enhanced since it is unclear what  $\alpha_{\text{cool}}$  originates from. Magnetohydrodynamic (MHD) turbulence producing the viscosity in the hot state is considered to be depressed in the quiescent disk due to much greater resistivity (Gammie & Menou 1998). Here, we consider the reason for the increase in viscosity in the case of constant mass transfer rates since our observations do not imply that mass transfer rates change during Event A. A change in the magnetic field of the secondary star, such as magnetic cycles and flaring events, may affect the angular momentum transport in the disk through turbulence or magnetized outflows and control the outburst behavior (Oláh et al. 2016; Scepi et al. 2020). Spiral density waves induced by tidal torques might contribute to  $\alpha_{\text{cool}}$  (Ju et al. 2016), but whether it is applicable to the quiescent disk in SS Cyg is in debate. Although it is proved that thermal convection can enhance the MHD turbulence, this is believed to be limited for the hot state (Hirose et al. 2014). Once the temperature is raised and the resistivity is lowered at a local region of the disk, the MHD turbulence begins to work and the disk temperature will increase because of enhanced dissipation, which further lowers the resistivity. Considering figure 1 of Gammie and Menou (1998), if  $\alpha_{\text{cool}}$  is enhanced and the cool branch of the thermal equilibrium curve shifts upwards, the resistivity seems to become weaker and the MHD turbulence may be switched on. Also, Sano and Stone (2002) investigated non-ideal MHD effects and showed that magnetorotational instability (MRI) operates if the magnetic Reynolds number exceeds a critical value. This transition may propagate over a wider region on the viscous timescale and the viscosity may be enhanced over the entire quiescent disk. Also, ionization of the gas at the upper layer of the disk may contribute to lowering the resistivity, though X-ray

<sup>14</sup> Here, we use the term “the cool state” instead of “the quiescent state” because we discuss the thermal state of the disk.

irradiation is not the main source of the increase in the optical flux. If the lower resistivity switches on MRI, the mass accretion rate is raised and the X-ray flux will increase. The irradiation effect then becomes stronger. However, it is unknown whether this kind of feedback loop and global transitions are feasible. This remains one of the future problems.

### 4.3 Nature of the 2021 anomalous event in SS Cyg

We here consider the origin of Event B in SS Cyg on the basis of the discussion in subsections 4.1 and 4.2. As described in subsection 4.1, we do not find any positive evidence for the enhancement of mass transfer rates during Event A. Also, the optical mean luminosity during Event B is comparable with that before Event B (see subsection 3.1), and hence the released energy from the disk via accretion does not seem to change drastically. Small-amplitude outbursts do not appear frequently with increasing mass transfer rates according to Cannizzo (1993a). We therefore investigate how we can explain the anomalous event in 2021 without variations of mass transfer rates.

X-ray irradiation of the disk and the secondary star is not enough to increase the optical flux by  $\sim 2$  mag when considering the observed X-ray flux (see table 1). The increment of the temperature of the secondary star by irradiation would only be  $\sim 6\%$  at most in Event B according to equation (4). The optical luminosity increases only by  $\sim 0.3$  mag at most by X-ray irradiation. Although it is possible that the secondary star is irradiated by the accretion disk, which is bright at optical and near-ultraviolet wavelengths, the disk flux must increase for this situation to occur. It is therefore natural to assume that the enhancement of viscosity in the cool state, which would be caused during Event A, is also related to the mechanism of Event B.

Mineshige and Osaki (1985) pointed out that the cooling and heating waves are easily trapped in a local region at which the thermal instability is triggered if  $\alpha_{\text{cool}}$  is equal to  $\alpha_{\text{hot}}$ . In their numerical simulations, the inner part of the disk always stays in the outburst state and the thermal instability arises at a local region in the outer part of the disk. The resultant light curve shows small-amplitude fluctuations. This phenomenon seems to be similar to Event B in SS Cyg. The  $B - V$  color during Event B may imply that the inner part of the disk is almost always in the outburst state. The  $V - I$  color during Event B may suggest that the outer part of the disk goes back and forth between the cool state and the hot state (see the squares in the left and right panels of figure 4). We suggest that  $\alpha_{\text{cool}}$  gradually approached  $\alpha_{\text{hot}}$  during the pre-stage in this system, causing Event B. Event B can be interpreted as consecutive low-amplitude outbursts

caused by the thermal instability triggered at the outer part of the disk.

Insufficient removal of the mass and angular momentum from the disk may also be involved in the cause of Event B. As discussed in subsection 4.2, the enhancement of  $\alpha_{\text{cool}}$  can increase the quiescent level, cause frequent low-amplitude and inside-out outbursts, and suppress long outbursts. A large amount of the disk mass is normally drained onto the WD in the long outburst and the mass accretion is not efficient in the short outburst (see figure 10 of Kimura et al. 2020b). It is considered that a larger amount of mass accumulated before the long outburst in 2021. The redder  $V - I$  color during Event A may suggest there was a mass reservoir in the cool outer disk (see the circles in the right panel of figure 4). The disk should have drained a lot of mass onto the WD during the long outburst in 2021 January. However, this long outburst showed a shoulder-like precursor at the beginning, which lasted for  $\sim 5$  d. Also, there was no clear plateau stage after the system reached the outburst maximum (see subsection 3.1). The plateau stage of the long outburst is considered to be generated by strong tidal torques on the outer disk edge when the disk reaches the tidal truncation radius, and the precursor is created before strong tidal torques begin to operate. The above-mentioned observational features thus suggest that the removal of the angular momentum of the disk by tidal torques during this long outburst was inefficient and that a lot of mass may remain in the disk even after this outburst was quenched around BJD 2459230. The remaining mass in the outer disk would be gradually consumed and help to maintain Event B. Although the multi-wavelength behavior around BJD 2459100 was similar to Event B, it was not long-lasting. This might be because the amount of disk mass stored before this phenomenon was smaller than that just before Event B.

### 4.4 Standstill-like phenomenon in SS Cyg-type stars and its relation to other types of standstills

As mentioned in the introduction, Event B at first appeared to be the same phenomenon as Z Cam-type standstill; however, our analyses suggest that this would be a group of small-amplitude outbursts. Event B is a standstill-like phenomenon at this stage rather than standstill, though the definition may be changed after the end of this phenomenon. Recently, a number of IW And-type DNe which repeat quasi-standstills terminated by small brightening have been discovered one after another. Here, quasi-standstills are intermediate brightness intervals with (damping) oscillations (e.g., Kato 2019; Lee et al. 2021). The thermal state of

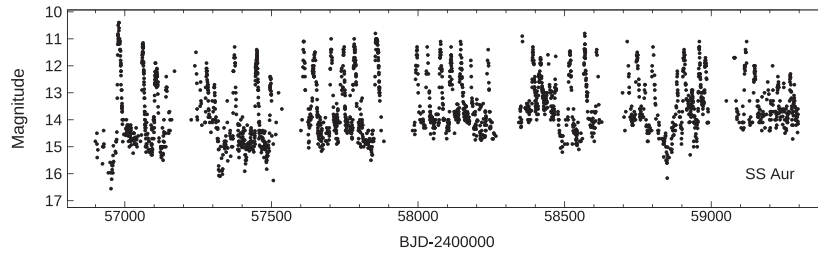


Fig. 9. Optical light curves of SS Aur, taken from the AAVSO archive. We use here the photometric data in the clear filter and the V band, along with visual observations.

the disk during Event B seems to resemble that during quasi-standstills in IW And-type DNe, which was investigated by Kimura et al. (2020b), rather than that during Z Cam-type standstill. According to their work, in IW And-type quasi-standstill, the inner disk is always in the hot state and the thermal instability is triggered in the outer disk, though it is unclear if this picture is true or not in light of recent observations (Kimura et al. 2020a).

We have noticed that some SS Cyg-type stars have entered a standstill or may show standstill-like phenomena like SS Cyg. For example, WW Cet experienced standstill in 2010. Moreover, its forerunner was a gradual increase in the optical flux in the quiescent state as in SS Cyg (see the top panel of figure E6). Additionally, another bright SS Cyg-type star SS Aur has become more active these days and repeats low-amplitude outbursts. We see from figure 9 that the quiescent flux is gradually increasing in this system. This system may enter standstill or standstill-like phases as SS Cyg and WW Cet did, considering the similarity in the precursor events. TW Vir would also be in the same state as SS Aur. We give in figure E6 the light curves of some DNe which have shown long-lasting increases in the optical flux in the quiescent state. We suggest that SS Cyg-type stars with mass transfer rates lower than the critical rate may show standstill-like events if some critical conditions such as an enhancement of viscosity in the cool state and a large amount of accumulated mass in the outer disk are satisfied.

We consider that standstill or standstill-like phenomena in CVs can be classified into two types: Z Cam-type standstill and standstill-like phenomena in SS Cyg-type stars, which possibly link to IW And-type quasi-standstills. An increase of the quiescent level is seen in the latter, and not in the former. The entire disk is thermally stable in the former, while the outer part of the disk is thermally unstable in the latter. The critical condition of the former type is high mass transfer rates close to  $\dot{M}_{\text{crit}}$ , but that of the latter type is not.

#### 4.5 Evolution of the X-ray-emitting region

So far we have presented our interpretation of what happened to the accretion disk during Events A and B. Here,

we try to understand the time evolution of the BL. In the case of SS Cyg, the X-ray luminosity drops and the X-ray spectrum becomes softer in the optical outburst (Wheatley et al. 2003; McGowan et al. 2004; Ishida et al. 2009). This would be because the BL becomes optically thick due to a lot of mass provided from the inner disk edge (Narayan & Popham 1993; Patterson & Raymond 1985a, 1985b). In comparing our results with the observation presented by Wheatley, Mauche, and Mattei (2003), the hardness ratio was comparable with that in the optical quiescence throughout T1–T5. This means that the BL was an optically thin coronal flow during Events A and B. In fact,  $\dot{M}_{\text{in}}$  estimated by equation (5) is lower than the critical mass accretion rate at the inner disk edge ( $\dot{M}_{\text{in,crit}}$ ) above which the BL becomes optically thick.<sup>15</sup> It is known that the X-ray luminosity rises by a factor of around five just before/after an outburst in SS Cyg, probably corresponding to  $\dot{M}_{\text{in}}$  (e.g., Wheatley et al. 2003; McGowan et al. 2004). The BL might be barely optically thin in these time periods, since the X-ray luminosity became higher by about five times in T4 and T5 than in the normal quiescence.

We next attempt to interpret the time evolution of the properties of the coronal flow other than its luminosity. During the normal optical quiescence, the solid angle subtended by the reflector was more than 1 and the maximum temperature of the plasma was around 20 keV (McGowan et al. 2004; Ishida et al. 2009). By contrast, the reflection effect was weak in T1–T5. The maximum temperature of the corona was 1.5 times higher at T1–T3 and the high-temperature component seems to have increased. The maximum temperature dropped a little in T4 and T5, and the photoelectric absorption increased from T3 to T5. In particular, the spectrum at T5 suggests that part of the plasma was masked by some dense absorbers (see sub-subsection 3.4.2). Also, it is suggested that the disk inner edge was a little smaller in T1 and T2 in comparison with the estimates by Balman and Revnivtsev (2012) in the normal quiescence, but the inner region of the disk was still truncated. The

<sup>15</sup> According to equation (6.20b) in Warner (1995),  $\dot{M}_{\text{in,crit}}$  is around a few times  $10^{17} \text{ g s}^{-1}$  for SS Cyg. Here we use the binary parameters measured by Hill et al. (2017).

inner disk edge may extend down to the vicinity of the WD in T4 and T5 (see subsection 3.5).

To explain the significant reflection effect during the normal quiescence, the optically thin corona is believed to have been compact with respect to the WD radius (Ishida et al. 2009). The weak reflection in T1–T5 suggests that the corona greatly expanded, especially in the vertical direction, during Events A and B. Its scale height should exceed the WD radius, and this picture is similar to a coronal siphon flow as proposed by Meyer and Meyer-Hofmeister (1994). This would be consistent with an increase in the temperature of the corona. The higher the temperature of the corona, the higher the gas pressure and the larger the scale height. Also, the gas in the inner disk would be ionized during Event B, and the reflection effect by neutral material would be lower.

In T1–T3, the maximum temperature and the density of higher-temperature gas of the coronal flow increased, which can be attributed to two factors. One is the shrinkage of the inner disk edge. If the gas cooling is inefficient, the gas is possibly heated up to the virial temperature, defined as

$$T_{\text{vir}} \sim \frac{GM_1 m_p}{6k_B r_{\text{in}}}, \quad (7)$$

where  $m_p$  is the proton mass and  $k_B$  is the Boltzmann constant (Hellier 2001; Kato et al. 2008). The smaller the inner disk edge, the higher the maximum temperature (though the situation may not be simple, as mentioned in subsection 4.1). The second factor is an enhancement of the viscous friction rate in the corona. If the viscous heating rate increases, hot components in the coronal flow are supposed to increase.

The maximum temperature of the plasma decreased from T3 to T4. This change could be explained if we consider the increase in the density of the coronal flow. The density would be relatively low in T1 and T2 since  $\dot{M}_{\text{in}}$  was not supposed to be very high; then, the radiative cooling of the corona was not efficient. The corona can be heated up to the virial temperature in this case. By contrast, the contraction of the disk inner edge suggests that a larger amount of gas was conveyed from the disk inner edge to the corona in T4 and T5 a while after the system entered Event B. More mass might evaporate into the coronal flow from a wider area of the inner disk. In these time periods, the coronal density would become higher and the radiative cooling would become more efficient. Under this situation, the maximum temperature is supposed to drop. At the beginning of Event B, i.e., at T3, the density might not be so high as at T4 and T5.

It is difficult to understand what the intrinsic absorption of SS Cyg originates from. The mass-loss rate due to outflows in non-magnetic CVs is less than about 1%,

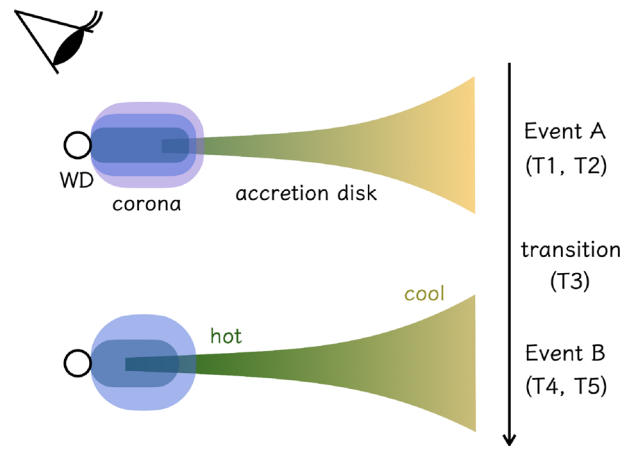


Fig. 10. Edge-on view of half of the entire accretion flow during Events A and B. Here, T1, T2, T3, T4, and T5 correspond to the time zones when the coordinated X-ray observations by NICER and NuSTAR were performed (see also figure 5). The purple region has a higher temperature than the blue region. (Color online)

and the outflows are observed only in the outburst state (Long & Knigge 2002). However, it may suggest that the SED modeling of the spectra in T5 is improved by using the model for partial photoelectric absorption (see also figure 5). As discussed by Done and Osborne (1997), part of the X-ray corona might be hidden from the observer by the optically thick disk, which extends down to the WD surface. Although the SEDs in T3 and T4 can be fitted well without partial absorption, the absorption by the disk may begin developing around T3 and T4. The increase in the absorption effect from T3 to T5 may suggest that the inner disk became optically thick, maintained the outburst state, and extended down to the WD surface during Event B.

We finally illustrate the entire accretion flow of SS Cyg during Events A and B in figure 10. The corona would be a multi-temperature plasma for all of the observations, and the corona and the inner part of the accretion disk would have a higher temperature than usual. The increase in accretion rates of the disk during Event A, which was probably caused by enhanced viscosity, might make the innermost disk radius contract a little and the maximum temperature of the corona higher. Then the coronal flow expanded vertically due to the high temperature. After T3, the accretion rate to the corona became much higher since the inner disk would enter the outburst state. As a larger amount of mass was provided to the corona, the inner edge of the disk gradually approached the WD surface, and the higher-density coronal flow was efficiently cooled down. It is controversial whether the disk is sandwiched by the coronal flow.



## 5 Summary

Since 2021 January SS Cyg has entered an unusual phenomenon possibly similar to standstill observed only in Z Cam-type stars. We observed this anomalous event and its multi-wavelength transition in this source at optical and X-ray wavelengths via the VSNET team, AAVSO, NICER, and NuSTAR. The main results are summarized as follows.

- The optical and X-ray flux gradually and simultaneously increased in the optical quiescent state before the anomalous event for  $\sim 500$  d. Also, small-amplitude outbursts frequently occurred in the pre-stage of the anomalous event.
- We found that the orbital hump was not amplified on average during the quiescent state in the pre-stage of the anomalous event in 2021.
- The  $B - V$  color suggests that the inner part of the disk would be hotter than usual during the quiescent state in the pre-stage and that the hot inner part might always be in the outburst state during the anomalous event. The  $V - I$  color suggests that a large amount of cool gas stored in the outer part of the disk and/or the disk expanded during the quiescent state in the pre-stage and during the anomalous event.
- The X-ray spectra during the optical quiescent state in the pre-stage and during the anomalous event are well expressed by a sum of bremsstrahlung emissivity. The reflection by the surface of the WD and/or the disk was less conspicuous than usual and the temperature of the BL became higher. The maximum temperature of the BL decreased in the middle of the anomalous event. The X-ray luminosity was higher than usual by  $\sim 2$ – $5$  times.
- The innermost disk radius estimated from the PSs of X-ray light curves is  $\sim 3.5 \times 10^9$  cm during quiescence in the pre-stage, which implies that the disk was truncated far from the WD surface. By contrast, the disk inner edge would extend down to the vicinity of the WD during the anomalous event.

We have investigated the cause of the anomalous phenomenon and its predecessor by the disk-instability model in the simple case where the mass transfer rate does not fluctuate since we have not found any positive evidence of a significant increase in mass transfer rates. X-ray irradiation was not the main source of the increase in the optical quiescent flux during the pre-stage. It is suggested that an increase in mass accretion rates of the disk, which would be caused by an enhancement of viscosity in the cool state, raised not only the optical flux but also the X-ray flux during the quiescent state. We also suggest that the anomalous event in 2021 was triggered by the enhancement of viscosity. During this event, the inner disk would always be in the outburst state and the thermal instability might work

only in the outer part of the disk. The anomalous event in 2021 in SS Cyg would be consecutive small outbursts and a standstill-like phenomenon. The combination of a simple case of the disk-instability model and increased viscosity in the quiescent disk could explain standstill and standstill-like phenomena in SS Cyg-type stars. The X-ray-emitting inner accretion flow would expand spatially because of the increase in its temperature. A slight decrease in the maximum temperature of the flow and the contraction of the innermost disk radius in the middle of the anomalous event seems to be consistent with the increase in accretion rates at the inner disk edge. Thus, the change in the accretion rate of the disk is likely to influence the structure and the temperature of the X-ray-emitting corona.

## Acknowledgments

We are thankful to the many amateur observers in VSNET, VSOLJ, and AAVSO, and Toshihiko Katayama, for providing a lot of data used in this research. We are grateful to the NuSTAR team for performing the ToO observations. We are grateful to Yoji Osaki who gave us a lot of insightful comments. We acknowledge Shigenobu Hirose, who commented on the origin of viscosity in the quiescent disk. M. Kimura is grateful to Yohei Nishino, Shigeyuki Sako, and Daisaku Nogami for discussing the data analyses. This work was financially supported by Japan Society for the Promotion of Science Grants-in-Aid for Scientific Research (KAKENHI) Grant Numbers JP20K22374 (MK), JP21K03616 (TK), JP20K14521 (KI), JP19K14762 (MS), and JP20H01941 (SY). M. Kimura acknowledges support by the Special Postdoctoral Researchers Program at RIKEN. The work by P. A. Dubovsky and I. Kudzej was supported by the Slovak Research and Development Agency under contract No. APVV-15-0458. We thank the anonymous referee for helpful comments.

## Supplementary data

The following supplementary data is available at [PASJ](https://academic.oup.com/pasj/article/73/5/1262/6329681) online: Tables E1–E4 and figures E1–E6.

## References

- Allan, A., Hellier, C., & Ramseyer, T. F. 1996, *MNRAS*, 282, 699  
 Aller, L. H. 1959, *PASP*, 71, 324  
 Anders, E., & Grevesse, N. 1989, *Geochim. Cosmochim. Acta*, 53, 197  
 Arévalo, P., & Uttley, P. 2006, *MNRAS*, 367, 801  
 Arnaud, K. A. 1996, in *ASP Conf. Ser.*, 101, *Astronomical Data Analysis Software and Systems V*, ed. G. H. Jacoby & J. Barnes (San Francisco: ASP), 17  
 Bailer-Jones, C. A. L., Rybizki, J., Fouesneau, M., Mantelet, G., & Andrae, R. 2018, *AJ*, 156, 58  
 Balman, Ş. 2020, *Adv. Space Res.*, 66, 1097  
 Balman, Ş., & Revnivtsev, M. 2012, *A&A*, 546, A112  
 Belloni, T., & Hasinger, G. 1990, *A&A*, 230, 103  
 Bruch, A. 1992, *A&A*, 266, 237

- Bruch, A. 2021, *MNRAS*, 503, 953
- Buat-Ménard, V., Hameury, J.-M., & Lasota, J.-P. 2001, *A&A*, 369, 925
- Cannizzo, J. K. 1993a, *ApJ*, 419, 318
- Cannizzo, J. K. 1993b, *Adv. Ser. Astrophys. Cosmology*, 9, 6
- Cannizzo, J. K. 2012, *ApJ*, 757, 174
- Cannizzo, J. K., & Mattei, J. A. 1998, *ApJ*, 505, 344
- Cannizzo, J. K., Shafter, A. W., & Wheeler, J. C. 1988, *ApJ*, 333, 227
- Cannizzo, J. K., Wheeler, J. C., & Polidan, R. S. 1986, *ApJ*, 301, 634
- Cleveland, W. S. 1979, *J. Am. Statist. Assoc.*, 74, 829
- Court, J. M. C., et al. 2020, *MNRAS*, 494, 4656
- Cruddace, R., Paresce, F., Bowyer, S., & Lampton, M. 1974, *ApJ*, 187, 497
- de Jong, J. A., van Paradijs, J., & Augusteijn, T. 1996, *A&A*, 314, 484
- Done, C., & Osborne, J. P. 1997, *MNRAS*, 288, 649
- Done, C., Osborne, J. P., & Beardmore, A. P. 1995, *MNRAS*, 276, 483
- Gammie, C. F., & Menou, K. 1998, *ApJ*, 492, L75
- Gendreau, K. C., et al. 2016, in *Proc. SPIE*, 9905, Space Telescopes and Instrumentation 2016: Ultraviolet to Gamma Ray, ed. J.-W. A. den Herder et al. (Bellingham, WA: SPIE), 99051H
- Hameury, J. M. 2020, *Adv. Space Res.*, 66, 1004
- Hameury, J. M., Knigge, C., Lasota, J. P., Hambach, F. J., & James, R. 2020, *A&A*, 636, A1
- Hameury, J. M., Menou, K., Dubus, G., Lasota, J.-P., & Hure, J.-M. 1998, *MNRAS*, 298, 1048
- Harrison, F. A., et al. 2013, *ApJ*, 770, 103
- Hellier, C. 2001, *Cataclysmic Variable Stars: How and Why They Vary* (Berlin: Springer)
- Hellier, C., Mukai, K., & Osborne, J. P. 1998, *MNRAS*, 297, 526
- Henden, A. A., Templeton, M., Terrell, D., Smith, T. C., Levine, S., & Welch, D. 2016, *VizieR Online Data Catalog*, 2336
- Hessman, F. V. 1986, *ApJ*, 300, 794
- Hessman, F. V., Robinson, E. L., Nather, R. E., & Zhang, E. 1984, *ApJ*, 286, 747
- Hill, C. A., Smith, R. C., Hebb, L., & Szkody, P. 2017, *MNRAS*, 472, 2937
- Hirose, S., Blaes, O., Krolik, J. H., Coleman, M. S. B., & Sano, T. 2014, *ApJ*, 787, 1
- Huppenkothen, D., et al. 2019, *ApJ*, 881, 39
- Ichikawa, S., & Osaki, Y. 1994, in *Theory of Accretion Disks – 2*, ed. W. J. Duschl et al. (Dordrecht: Kluwer Academic Publishers), 169
- Ishida, M., Okada, S., Hayashi, T., Nakamura, R., Terada, Y., Mukai, K., & Hamaguchi, K. 2009, *PASJ*, 61, 77
- Ju, W., Stone, J. M., & Zhu, Z. 2016, *ApJ*, 823, 81
- Kato, S., Fukue, J., & Mineshige, S. 2008, *Black-Hole Accretion Disks: Towards a New Paradigm* (Kyoto: Kyoto University Press)
- Kato, T. 2019, *PASJ*, 71, 20
- Kimura, M., Osaki, Y., & Kato, T. 2020a, *PASJ*, 72, 94
- Kimura, M., Osaki, Y., Kato, T., & Mineshige, S. 2020b, *PASJ*, 72, 22
- Lee, C.-D., et al. 2021, *ApJ*, 911, 51
- Long, K. S., & Knigge, C. 2002, in *ASP Conf. Ser.*, 261, The Physics of Cataclysmic Variables and Related Objects, ed. B. T. Gänsicke et al. (San Francisco: ASP), 327
- Lyubarskii, Y. E. 1997, *MNRAS*, 292, 679
- McGowan, K. E., Priedhorsky, W. C., & Trudolyubov, S. P. 2004, *ApJ*, 601, 1100
- Madsen, K. K., Grefenstette, B. W., Pike, S., Miyasaka, H., Brightman, M., Forster, K., & Harrison, F. A. 2020, *arXiv:2005.00569*
- Matsuoka, M., et al. 2009, *PASJ*, 61, 999
- Mauche, C. W., Raymond, J. C., & Cordova, F. A. 1988, *ApJ*, 335, 829
- Meyer, F., & Meyer-Hofmeister, E. 1981, *A&A*, 104, L10
- Meyer, F., & Meyer-Hofmeister, E. 1983, *A&A*, 121, 29
- Meyer, F., & Meyer-Hofmeister, E. 1994, *A&A*, 288, 175
- Mineshige, S., & Osaki, Y. 1985, *PASJ*, 37, 1
- Mineshige, S., & Wood, J. H. 1989, *MNRAS*, 241, 259
- Nakaniwa, N., Hayashi, T., Takeo, M., & Ishida, M. 2019, *MNRAS*, 488, 5104
- Narayan, R., & Yi, I. 1994, *ApJ*, 428, L13
- Narayan, R., & Popham, R. 1993, *Nature*, 362, 820
- Nauenberg, M. 1972, *ApJ*, 175, 417
- Oláh, K., Kővári, Zs., Petrovay, K., Soon, W., Baliunas, S., Kolláth, Z., & Vida, K. 2016, *A&A*, 590, A133
- Osaki, Y. 1996, *PASP*, 108, 39
- Osaki, Y., & Meyer, F. 2004, *A&A*, 428, L17
- Patterson, J., & Raymond, J. C. 1985a, *ApJ*, 292, 535
- Patterson, J., & Raymond, J. C. 1985b, *ApJ*, 292, 550
- Provenzal, J. L., Shipman, H. L., Høg, E., & Thejll, P. 1998, *ApJ*, 494, 759
- Ramsay, G., Cannizzo, J. K., Howell, S. B., Wood, M. A., Still, M., Barclay, T., & Smale, A. 2012, *MNRAS*, 425, 1479
- Revnivtsev, M., et al. 2010, *A&A*, 513, A63
- Ritchey, A. M., Wallerstein, G., & McKeever, J. 2013, *PASP*, 125, 1429
- Ross, J., & Latter, H. N. 2017, *MNRAS*, 470, 34
- Sano, T., & Stone, J. M. 2002, *ApJ*, 577, 534
- Scaringi, S. 2014, *MNRAS*, 438, 1233
- Scepi, N., Lesur, G., Dubus, G., & Jacquemin-Ide, J. 2020, *A&A*, 641, A133
- Schreiber, M. R., Hameury, J.-M., & Lasota, J.-P. 2003, *A&A*, 410, 239
- Smak, J. 1984, *Acta Astron.*, 34, 161
- Tsujimoto, M., Morihana, K., Hayashi, T., & Kitaguchi, T. 2018, *PASJ*, 70, 109
- Uttley, P., & McHardy, I. M. 2001, *MNRAS*, 323, L26
- Waagen, E. O. 2020, *AAVSO Alert Notice*, 720, 1
- Warner, B. 1995, *Cataclysmic Variable Stars* (Cambridge: Cambridge University Press)
- Wheatley, P. J., Mauche, C. W., & Mattei, J. A. 2003, *MNRAS*, 345, 49
- Wood, J., Horne, K., Berriman, G., Wade, R., O'Donoghue, D., & Warner, B. 1986, *MNRAS*, 219, 629
- Xu, X.-J., Yu, Z.-L., & Li, X.-D. 2019, *ApJ*, 878, 53
- Yonehara, A., Mineshige, S., & Welsh, W. F. 1997, *ApJ*, 486, 388